AGU PUBLICATIONS

JGR

Journal of Geophysical Research: Solid Earth

RESEARCH ARTICLE

10.1002/2016JB013352

Key Points:
- Single-crystal elastic constants of ferropericlase were measured at high P-T
- Lateral heterogeneity in a pyrolite aggregate has been determined along geotherm
- Thermally induced lateral heterogeneity dominates the upper lower mantle

Supporting Information:
- Table S1
- Figure S1

Correspondence to:
J.-F. Lin,
afu@jsg.utexas.edu

Citation:
Yang, J., J.-F. Lin, S. D. Jacobsen, N. M. Seymour, S. N. Tkachev, and V. B. Prakapenka (2016), Elasticity of ferropericlase and seismic heterogeneity in the Earth's lower mantle, *J. Geophys. Res. Solid Earth*, *121*, 8488–8500, doi:10.1002/2016JB013352.

Received 11 JUL 2016
Accepted 20 NOV 2016
Accepted article online 22 NOV 2016
Published online 16 DEC 2016

Elasticity of ferropericlase and seismic heterogeneity in the Earth's lower mantle

HPSTAR 324-2016

Jing Yang[1], Jung-Fu Lin[1,2], Steven D. Jacobsen[3], Nikki M. Seymour[1], Sergey N. Tkachev[4], and Vitali B. Prakapenka[4]

[1]Department of Geological Sciences, Jackson School of Geosciences, University of Texas at Austin, Austin, Texas, USA, [2]Center for High Pressure Science and Technology Advanced Research (HPSTAR), Shanghai, China, [3]Department of Earth and Planetary Sciences, Northwestern University, Evanston, Illinois, USA, [4]Center for Advanced Radiation Sources, University of Chicago, Chicago, Illinois, USA

Abstract Deciphering the origin of seismic heterogeneity has been one of the major challenges in understanding the geochemistry and geodynamics of the deep mantle. Fully anisotropic elastic properties of constituent minerals at relevant pressure-temperature conditions of the lower mantle can be used to calculate seismic heterogeneity parameters in order to better understand chemically and thermally induced seismic heterogeneities. In this study, the single-crystal elastic properties of ferropericlase ($Mg_{0.94}Fe_{0.06}$)O were measured using Brillouin spectroscopy and X-ray diffraction at conditions up to 50 GPa and 900 K. The velocity-density results were modeled using third-order finite-strain theory and thermoelastic equations along a representative geotherm to investigate high pressure-temperature and compositional effects on the seismic heterogeneity parameters. Our results demonstrate that from 660 to 2000 km, compressional wave anisotropy of ferropericlase increased from 4% to 9.7%, while shear wave anisotropy increased from 9% to as high as 22.5%. The thermally induced lateral heterogeneity ratio ($R_{S/P} = \partial \ln V_S / \partial \ln V_P$) of ferropericlase was calculated to be 1.48 at ambient pressure but decreased to 1.43 at 40 GPa along a representative geotherm. The $R_{S/P}$ of a simplified pyrolite model consisting of 80% bridgmanite and 20% ferropericlase was approximately 1.5, consistent with seismic models at depths from 670 to 1500 km, but showed an increased mismatch at lower mantle depths below ~1500 km. This discrepancy below mid-lower mantle could be due to either a contribution from chemically induced heterogeneity or the effects of the Fe spin transition in the deeper parts of the Earth's lower mantle.

1. Introduction

Seismic heterogeneities within the Earth's lower mantle are typically attributed to thermal and/or chemical variations of the constituent materials [*Karato and Karki*, 2001]. Some authors have suggested that heterogeneity of the lower mantle is dominantly due to thermal effects [*Forte*, 2000; *Forte et al*., 1994; *Hager et al*., 1984], while chemical heterogeneity has been invoked by other studies to explain large low-shear-velocity provinces (LLSVPs) in the lowermost mantle beneath the Pacific and African plates [*Garnero and McNamara*, 2008; *van der Hilst and Kárason*, 1999]. A more recent study has proposed a combined thermochemical mechanism for the development of the seismic structure of LLSVPs based on their long-wavelength structure, lateral shear-velocity anisotropy, sharp velocity gradients along their margins, and anticorrelated bulk and shear velocities [*Davies et al*., 2015]. Distinguishing between the thermal and chemical contributions to seismic heterogeneities of the lower mantle from a material properties perspective is critical as each mechanism has drastically different implications for our understanding of the geodynamics, geochemistry, and thermal evolution of the planet's interior. Our present understanding of the origin of the lateral heterogeneity in the lower mantle minerals remains mostly theoretical [*Tsuchiya*, 2011; *Wu and Wentzcovitch*, 2014]. However, comparisons of lateral variations in seismic shear wave (V_S) and compressional wave (V_P) velocities, given as $R_{S/P} = \partial \ln V_S / \partial \ln V_P$, in conjunction with mineral physics elasticity experiments on lower mantle minerals at relevant pressure-temperature (P-T) conditions, can provide new constraints on the lower mantle seismic structures and dynamics.

Based on the pyrolite model, Earth's lower mantle, the most voluminous layer of the planet, consists of approximately 75% bridgmanite (Mg,Fe)SiO_3, 20% ferropericlase (Mg,Fe)O, and 5% Ca-silicate perovskite ($CaSiO_3$) [*Ringwood*, 1975]. Accurate determinations of the elastic properties of deep Earth materials under the relevant P-T conditions are essential for understanding seismic models of the deep mantle. It has been

suggested that variations in mineralogy, Fe or Al content of bridgmanite, and Fe spin states are plausible candidates for lateral heterogeneity in Earth's lower mantle [*Jackson et al*., 2005; *McCammon et al*., 2008]. Changes in the elasticity and texture of ferropericlase, including the effects of the spin transition, have also been proposed as potential sources of mid-lower mantle seismic heterogeneities [*Karato and Karki*, 2001; *Wu and Wentzcovitch*, 2014]. The elasticity of ferropericlase with varying Fe content has been experimentally and theoretically studied at lower mantle pressures across the spin transition, showing that V_P is significantly reduced while *Vs* remains unaffected over the transition [*Marquardt et al*., 2009; *Wu et al*., 2013; *Wu and Wentzcovitch*, 2014; *Yang et al*., 2015]. Ferropericlase is a rheologically weaker phase compared to bridgmanite and can develop a strong lattice preferred orientation, producing shear wave anisotropy $V_{SH} > V_{SV}$ (where V_{SH} and V_{SV} are the velocities of the horizontally and vertically polarized seismic shear waves, respectively) in the lower mantle [*Yamazaki and Karato*, 2002]. However, the contribution of ferropericlase to the thermal and chemical heterogeneities has remained theoretical. Fully resolving its density, elastic constants, and bulk and shear moduli under high P-T conditions is critical to rigorously test theoretical calculations against experimental data and explicitly elucidate the thermal and chemical variations in the lower mantle.

Here we have measured the acoustic wave velocities and density of synthetic single-crystal ferropericlase [$(Mg_{0.96}F_{0.06})O$] at high P-T conditions up to 50 GPa and 900 K using Brillouin light scattering (BLS) combined with X-ray diffraction (XRD) in an externally heated diamond anvil cell (EHDAC). Using these data, we have calculated elastic and seismic properties of ferropericlase along a representative lower mantle geotherm and discuss the potential contribution of ferropericlase on seismic heterogeneities of the lower mantle.

2. Experimental Methods

Single-crystal ferropericlase with $X\mathrm{Fe} = \mathrm{Fe}/(\mathrm{Mg}+\mathrm{Fe}) = 0.06$ ($(Mg_{0.94}Fe_{0.06})O$, hereafter denoted as fp6) was synthesized through the interdiffusion of Fe and Mg between single-crystal periclase (MgO) and prereacted (Mg,Fe)O powders [*Jacobsen et al*., 2002]. The ferric-iron content $Fe^{3+}/\mathrm{SFe} = 0.02(1)$; density $\rho_0 = 3723\ \mathrm{kg/m^3}$; and other details of synthesis, structure, and elastic properties of the sample at ambient conditions were reported by *Jacobsen et al*. [2002]. For high P-T Brillouin and XRD measurements, thin plates of the single-crystal ferropericlase were polished on both sides perpendicular to [100] to ~12 μm in thickness and then cleaved into several ~70 × 70 μm square pieces. Single-crystal XRD patterns with an incident X-ray wavelength of 0.3344 Å were used to determine sample orientation and density at beamline 13-BMD in GeoSoilEnviroConsortium for Advanced Radiation Sources (GSECARS) of the Advanced Photon Source, Argonne National Laboratory (APS, ANL). Re-W alloy, which is more stable at high temperatures than a typical Re gasket, was used as the gasket material for high P-T experiments. A 250 μm thick gasket was preindented to ~30–40 μm by a pair of diamonds with a 300 μm culet size in an EHDAC [*Kantor et al*., 2012]. A hole of 170 μm was subsequently drilled and used as sample chamber. The ferropericlase crystal was loaded into the EHDAC sample chamber together with Au powder, which served as the pressure calibrant at high P-T [*Fei et al*., 2007], and an ~5 μm ruby sphere, used as the pressure indicator for loading Ne gas pressure medium. The temperature of the sample in the EHDAC was measured using an R-type thermocouple attached to one of the diamond anvils approximately 500 μm away from the diamond culet. The EHDAC was equipped with an alumina ceramic heater coiled with two pieces of Pt wire of 200 μm diameter and 48 cm in length [*Kantor et al*., 2012]. Four experimental runs at GSECARS were conducted over a 2 year period totaling ~60 8 h shifts to collect the data presented here.

High P-T Brillouin measurements were conducted at stepwise pressures up to 50 GPa at 4 constant temperatures of 300 K, 550 K, 750 K, and 900 K at 13 BMD in GSECARS of the APS, ANL. To avoid potential oxidation of the diamond anvils and Pt wires at high temperature, Ar gas with 2% H_2 gas continuously flowed into the EHDAC during heating. A solid state Verdi V2 laser with a wavelength of 532 nm and a power of 0.4 W was used for Brillouin measurements. Brillouin spectra were collected in asymmetric forward scattering geometry with an external scattering angle of 50° using a six-pass tandem Fabry-Perot interferometer. The acoustic velocities of the Brillouin spectra were derived from the measured Brillouin frequency shift as follows:

$$V_{P,S} = \frac{\lambda_0 \Delta v_B}{2\sin(\theta/2)}, \tag{1}$$

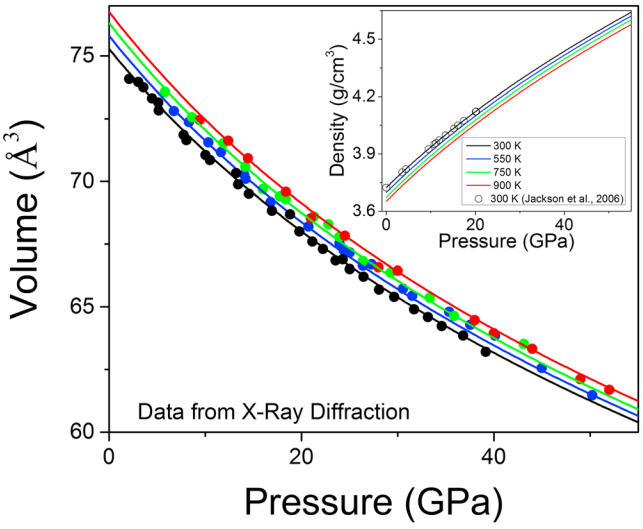

Figure 1. Pressure-volume-temperature relations of single-crystal ferropericlase ($Mg_{0.94}Fe_{0.06}$)O from X-ray diffraction. The solid symbols are the experimental measurements at 300 K (black), 550 K (blue), 750 K (green), and 900 K (red). The lines are the fits to experimental data using the third-order Birch-Murnaghan equation of state. The inset shows the density of the ferropericlase as a function of pressure. The open circles are from *Jackson et al.* [2006].

where $V_{P,S}$ is the measured acoustic velocity, λ_0 is the laser wavelength of 532 nm, $\Delta\nu_B$ is the Brillouin frequency shift, and θ is the external scattering angle of 50°. The Brillouin spectra were collected along principle axes [100] and [110] of single-crystal ferropericlase platelet, which were confirmed by in situ XRD patterns of the crystal before the measurements. XRD patterns of the ferropericlase at each given P-T were also used to determine the density (ρ) of the sample. The elastic constants (C_{11}, C_{12}, and C_{44}) of ferropericlase were determined using the following equations via least squares regression:

$$V_P\,[100] = (C_{11}/\rho)^{1/2}, \quad (2)$$

$$V_S[100] < 110 > = (C_{44}/\rho)^{1/2}, \quad (3)$$

$$V_P\,[110] = [(C_{11} + C_{12} + 2C_{44})/2\rho]^{1/2}, \quad (4)$$

$$V_S\,[110] < 110 > = [(C_{11} - C_{12})/2\rho]^{1/2}, \quad (5)$$

where [*uvw*] represents the crystallographic direction of acoustic wave propagation, and <*uvw*> indicates the polarization direction. Pressure was determined from the measured lattice parameter of Au and calibrated using the thermal equation of state [*Fei et al.*, 2007]. Pressure was measured before and after each Brillouin measurement, and the average pressure was used in the equation of state fitting. Errors are given by their standard deviation (1σ).

3. Results and Thermoelastic Modeling

High P-T XRD patterns of the single-crystal ferropericlase ($Mg_{0.94}Fe_{0.06}$)O were collected up to 50 GPa at temperatures of 300 K, 550 K, 750 K, and 900 K (Figure 1). The lattice parameters of ferropericlase were calculated based on four sets of diffraction peaks corresponding to {200}, {220}, {400}, and {420} equivalent reflections. Analysis of the XRD patterns of the sample also confirmed that the crystal was oriented in the (100) crystallographic plane within approximately ±1° angular uncertainty at high P-T. The *P-V* curves at each temperature were fitted using the third-order Birch-Murnaghan equation of state [*Birch*, 1947]. The calculated density as a function of pressure at 300 K was consistent with values reported by *Jackson et al.* [2006] (Figure 1 inset). The thermal expansion coefficient α was calculated using

$$V(T) = V_0 \exp\left[\int_{T_0}^{T} \alpha(T)dT\right], \quad (6)$$

where V_0 is the volume at 300 K and $\alpha(T)$ is a constant at ambient pressure, with a value of $3.0\,(1)\times10^{-5}\,K^{-1}$, determined by fitting the experimental data at ambient pressure. The pressure derivative of the thermal expansion coefficient $\left(\frac{\partial\alpha(T)}{\partial P}\right)$ is approximately $-1.0\times10^{-7}\ K^{-1}\ GPa^{-1}$.

High P-T Brillouin spectra of ferropericlase along the [100] and [110] crystallographic directions are shown in Figure 2. Most of the Brillouin spectra showed strong V_P and V_S peaks with high signal-to-noise ratios at high

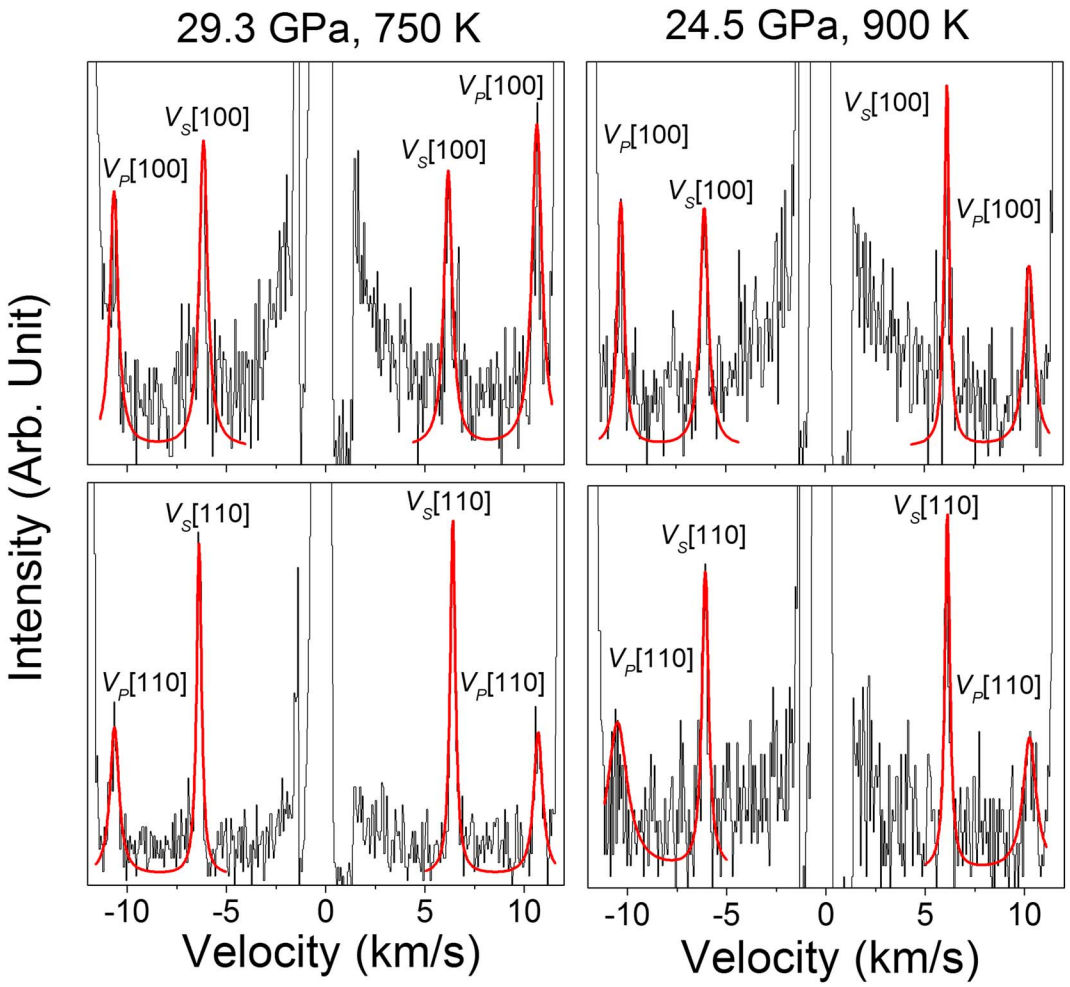

Figure 2. Representative Brillouin spectra of single-crystal ferropericlase $(Mg_{0.94}Fe_{0.06})O$ at high pressure and temperature. Black line: collected raw data; red line: Lorentz peak fit. (top) Velocity measured along [100] crystallographic direction and (bottom) velocity measured along [110] crystallographic direction.

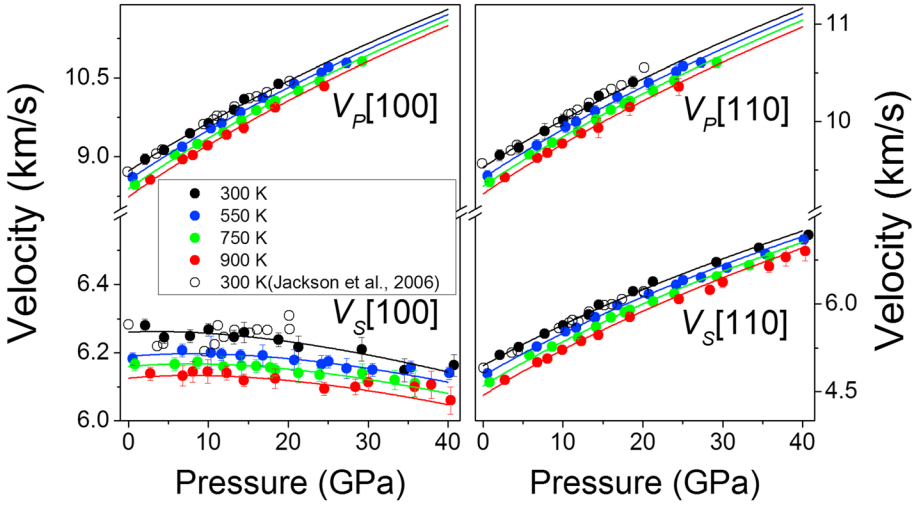

Figure 3. Acoustic velocities of the single-crystal ferropericlase $(Mg_{0.94}Fe_{0.06})O$ along (left) [100] and (right) [110] crystallographic directions as a function of pressure and temperature. The lines are calculated from modeled results of the elastic constants using finite-strain theory (see Figure 3 for further details). Solid circles: this study; open circles: $(Mg_{0.94}Fe_{0.06})O$ crystal along same crystallographic directions reported by *Jackson et al*. [2006].

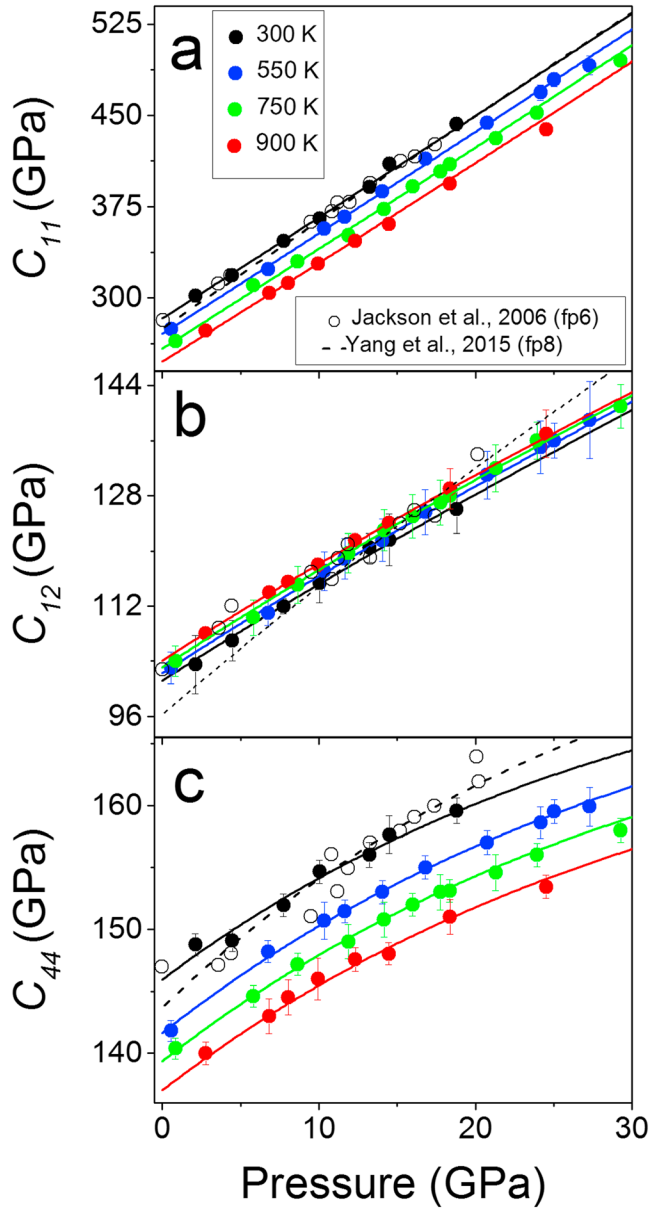

Figure 4. (a–c) Elastic constants of the single-crystal ferropericlase $(Mg_{0.94}Fe_{0.06})O$ as a function of pressure and temperature. The solid lines are the fitted results with a third-order finite-strain equation. Open circles: *Jackson et al.* [2006]; dashed lines: *Yang et al.* [2015].

P-T. The V_P mode of ferropericlase overlapped with the V_S of diamond in the anvils above ~30 GPa, preventing measurement of V_P at these conditions. V_P and V_S modes as a function of pressure at each temperature along the [100] and [110] directions are shown in Figure 3. These velocities increase with increasing pressure except for V_S[100]<110>, which remains almost constant up to ~10 GPa before decreasing with increasing pressure. The velocities as a function of pressure at a constant temperature of 300 K are consistent with those reported for fp6 by *Jackson et al.* [2006]. Together with the density information at high P-T from XRD measurements, the measured V_P and V_S velocities of the single-crystal ferropericlase permit direct derivation of the full elastic tensor at high P-T via equations 2–5 (Figure 4) [*Every*, 1980].

Elastic constants of the single-crystal ferropericlase $(Mg_{0.94}Fe_{0.06})O$ at ambient pressure as a function of experimental temperatures are shown in Table 1 and compared with literature results in Table 2. The pressure and temperature derivatives of the reference elastic moduli, as shown in Table 3, were obtained by fitting the moduli either at constant T, using the third-order Eulerian finite-strain equation (Figure 4) [*Birch*, 1978], or at constant P, using linear equation:

$$C_{ij}^0(T) = C_{ij}^0(300\ \mathrm{K}) + (T-300)\left(\partial C_{ij}/\partial T\right)_P, \quad (7)$$

$$C_{ij}(f) = (1+2f)^{7/2}\left[C_{ij}^0 + b_1 f + (1/2)b_2 f^2\right] - Pb_3, \quad (8)$$

Table 1. Elastic Moduli of Single-Crystal Ferropericlase $(Mg_{0.94}Fe_{0.06})O$ at Ambient Pressure as a Function of Experimental Temperatures

	K_{S0} (GPa)	G_0 (GPa)	C_{11} (GPa)	C_{12} (GPa)	C_{44} (GPa)
300 K	160(2)	121(1)	283(3)	101(2)	146(2)
550 K	157(2)	116(1)	270(4)	102(2)	142(2)
750 K	153(3)	112(2)	258(4)	103(2)	139(2)
900 K	151(3)	108(2)	248(4)	104(3)	137(2)

Table 2. Comparison of the Elastic Moduli at Ambient Conditions

	Composition	K_{S0} (GPa)	G_0 (GPa)	C_{11} (GPa)	C_{12} (GPa)	C_{44} (GPa)
This study	$(Mg_{0.94}Fe_{0.06})O$	160(2)	121(1)	283(3)	101(2)	146(2)
Jackson et al. [2006]	$(Mg_{0.94}Fe_{0.06})O$	163(3)	121(2)	284(3)	103(1)	147(1)
Jacobsen et al. [2002]	$(Mg_{0.94}Fe_{0.06})O$	161(3)	121(2)	281(2)	101(2)	147(1)
Marquardt et al. [2009]	$(Mg_{0.9}Fe_{0.1})O$	164(1)	116(1)	280(1)	102(1)	142(1)
Sinogeikin and Bass [2000]	MgO	163.2(10)	130.2(10)	297.9(15)	95.8(10)	154.4(20)
Karki et al. [1997][a]	MgO	158	121.8	291	91	139

[a]Theoretical calculation

$$b_1 = 3K_{S0}\left(C'^{0}_{ij} - b_3\right) - 7C^0_{ij}, \tag{9}$$

$$b_2 = 3K'_{S0}\left(b_1 + 7C^0_{ij}\right) - 16b_1 - 49C^0_{ij}, \tag{10}$$

$$f = (1/2)\left[(V_0/V)^{\frac{2}{3}} - 1\right]. \tag{11}$$

where $C^0_{ij}(300\,\mathrm{K})$ is the derived elastic constant from measurements at ambient pressure and temperature (300 K) and is thus fixed for the further modeling; $C^0_{ij}(T)$ is the elastic constant at high temperature and ambient pressure; C^0_{ij} and C'^{0}_{ij} is the elastic constant at ambient conditions and its first pressure derivative, respectively; and V_0 and V are the unit-cell volumes at ambient conditions and at high pressures, respectively.

Using the derived elastic constants of the sample, the aggregate adiabatic bulk (K_S) and shear moduli (G) were calculated using the Voigt-Ruess-Hill averages [*Hill*, 1952] (Figures 5a and 5b):

$$K_S = C_{11} - 2C/3, \tag{12}$$

$$G = \left[\left(C/5 + {}^{3C_{44}}/_{5}\right) + 5C_{44}C/(4C_{44} + 3C)\right]/2, \tag{13}$$

$$C = C_{11} - C_{12}. \tag{14}$$

The derived K_{S0} and G_0 at ambient conditions are 160(2) GPa and 121(1) GPa, respectively, which are fixed for further thermoelastic modeling. The aggregate velocities of the sample (Figures 5c and 5d) are calculated using the equations

$$V_P = \sqrt{{(K_S + 4G/3)}/{\rho}}, \tag{15}$$

$$V_S = \sqrt{G/\rho}. \tag{16}$$

Table 3. Comparison of the Temperature and Pressure Derivatives of the Single-Crystal Elastic Moduli of Ferropericlase

Temperature Derivatives	Composition	$(\partial K_S/\partial T)_P$ (MPa/K)	$(\partial G/\partial T)_P$ (MPa/K)	$(\partial C_{11}/\partial T)_P$ (MPa/K)	$(\partial C_{12}/\partial T)_P$ (MPa/K)	$(\partial C_{44}/\partial T)_P$ (MPa/K)
This study	$(Mg_{0.94}Fe_{0.06})O$	−15.4(1.1)	−21.3(9)	−58.1(2.2)	4.9(4)	−15.1(4)
Karki et al. [1999][a]	MgO	−14.0	−21.6	−59.8	8.9	−8.8
Wu and Wentzcovitch [2014][a]	$(Mg_{0.875}Fe_{0.125})O$	−12	−11			
Pressure derivatives	**Composition**	$(\partial K_S/\partial P)_T$	$(\partial G/\partial P)_T$	$(\partial C_{11}/\partial P)_T$	$(\partial C_{12}/\partial P)_T$	$(\partial C_{44}/\partial P)_T$
This study	$(Mg_{0.94}Fe_{0.06})O$	4.0(2)	2.1(1)	8.3(2)	1.5(1)	1.0(1)
Jackson et al. [2006]	$(Mg_{0.94}Fe_{0.06})O$	3.9(2)	2.1(1)	8.35	1.42	0.89
Yang et al. [2015]	$(Mg_{0.92}Fe_{0.08})O$			8.99(0.1)	1.95(0.12)	1.22(0.1)
Marquardt et al. [2009]	$(Mg_{0.9}Fe_{0.1})O$	3.98(14)		8.71(15)	1.74(14)	0.84(18)
Jacobsen et al. [2005]	$(Mg_{0.76}Fe_{0.24})O$	4.17	2.7(1)	9.3(2)	1.3(6)	1.2(1)
Jacobsen et al. [2005]	$(Mg_{0.44}Fe_{0.56})O$	4.17	1.5(1)	9.6(4)	1.5(4)	−0.16(9)
Sinogeikin and Bass [2000]	MgO	4.0(1)	2.4(1)	9.05(20)	1.34(15)	0.84(20)
Karki et al. [1999][a]	MgO	4.15	2.44	9.56	1.45	1.03

[a]Theoretical calculations.

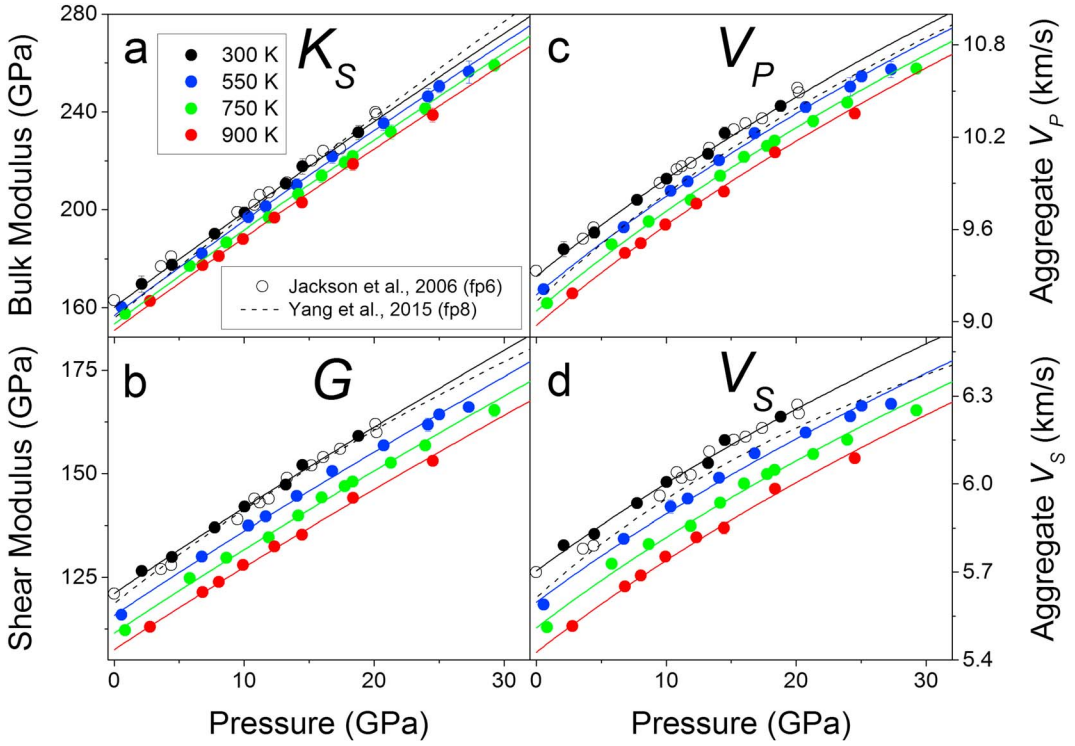

Figure 5. (a–d) Aggregate elastic moduli and velocities of ferropericlase $(Mg_{0.94}Fe_{0.06})O$ as function of pressure and temperature. The solid lines are the fits to experimental data using a third-order finite-strain equation. Open circles: *Jackson et al.* [2006]; dashed lines: *Yang et al.* [2015].

The P-T derivatives of the reference isotropic elastic moduli were obtained by fitting the moduli either at constant T, using the third-order Eulerian finite-strain equations [*Birch*, 1978], or at constant P using linear equation:

$$K_{S0}(T) = K_{S0}(300\ \mathrm{K}) + (T - 300)(\partial K_S/\partial T)_P, \tag{17}$$

$$K_S = K_{S0}(1+2f)^{5/2}\left\{1 + \left[3K'_{S0} - 5\right]f + 1/2\left[9K'^{\,2}_{S0} - 36K'_{S0} + 35\right]f^2\right\}, \tag{18}$$

$$G_0(T) = G_0(300\ \mathrm{K}) + (T - 300)(\partial G/\partial T)_P, \tag{19}$$

$$G = (1+2f)^{5/2}\left\{G_0 + \left[3G'_0K_{S0} - 5G_0\right]f + 9\left[K^2_{S0}\left[(1/K_{S0})\left(K'_{S0} - 4G'_0\right)\right] + 35G_0/9\right]f^2\right\}, \tag{20}$$

where K_{S0} and G_0 are the derived elastic moduli from measurements with ambient pressure and temperature (300 K), $K_{S0}(T)$ and $G_0(T)$ are the elastic moduli at high temperature and ambient pressure, K'_{S0} and G'_0 are the first pressure derivatives of the elastic moduli, and f is the Eulerian strain. A self-consistent density model was adopted to determine the finite-strain parameters for elastic moduli [*Speziale and Duffy*, 2002]. Densities from the XRD results were first used for the initial finite-strain fitting. The derived K_S and K'_{S0} were converted to the isothermal bulk modulus (K_T) and its pressure derivative at constant temperature K'_{T0} using the following thermodynamic relations [*Poirier*, 2000]:

$$K_{T0} = K_{S0}/(1 + \alpha_0\gamma_{0T}T), \tag{21}$$

$$K'_{T0} \cong (1 + \alpha_0\gamma_0 T)^{-1}\left[K'_{S0} - \left(\frac{\gamma_0 T}{K_{T0}}\right)(\partial K_T/\partial T)_{P0}\right], \tag{22}$$

where $(\partial K_T/\partial T)_{P0}$ is the temperature derivative of K_T at ambient pressure, K_{T0} is the isothermal bulk modulus at ambient conditions, α_0 is the thermal expansion coefficient, and γ_0 is the Grüneisen parameter. The isothermal parameter K'_{T0} was then used to fit the *P-V-T* relation to obtain refined density. The procedure was iterated until both K_T and K'_{T0} values were convergent and self-consistent with the input *P-V-T* relation.

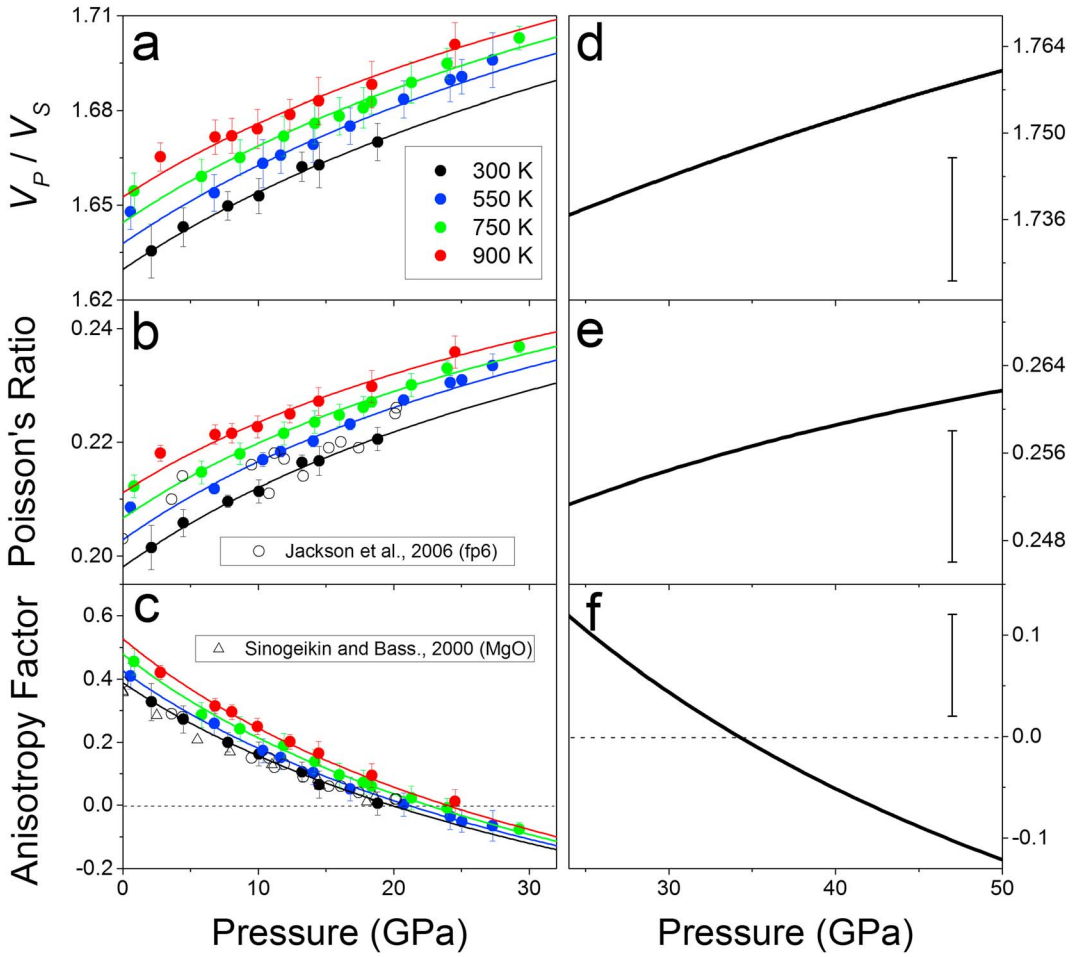

Figure 6. Seismic parameters of single-crystal ferropericlase $(Mg_{0.94}Fe_{0.06})O$ as a function of pressure and temperature. (a) V_P/V_S ratio, (b) Poisson's ratio, and (c) anisotropy factor. The anisotropy factor is defined as $A = [(2C_{44} + C_{12})/C_{11}] - 1$. The lines are calculated from fitted results of the elastic constants and moduli (see Figures 3 and 4 for these parameters). Open circles: *Jackson et al.* [2006]; triangles: *Sinogeikin and Bass* [2000]. (d) V_P/V_S ratio, (e) Poisson's ratio, and (f) anisotropy factor along an expected geotherm of the lower mantle [*Brown and Shankland*, 1981]. The representative error bars are estimated using standard error propagation from the modeled parameters.

Thermoelastic results from XRD are used to derive for these parameters: $(\partial K_T/\partial T)_{P0} = -0.01\,\mathrm{GPa\,K^{-1}}$ and $\alpha_0 = 3.0 \times 10^{-5}\,\mathrm{K^{-1}}$ at 300 to 900 K temperature conditions. The literature value $\gamma_{0T} = 1.443$ is used for the conversion [*Tange et al.*, 2009].

4. Discussion and Implications

4.1. High-Temperature Effects on the Seismic Parameters of Ferropericlase

Knowledge of the elastic anisotropy (A), Poisson's ratio (υ), and V_P/V_S ratio of ferropericlase at high P-T may shed light on understanding seismic anisotropy within the Earth's lower mantle. For the cubic ferropericlase, the elastic anisotropy factor (A) can be expressed as

$$A = \frac{2C_{44} + C_{12}}{C_{11}} - 1. \tag{23}$$

The Poisson's ratio (υ) can be expressed as

$$\upsilon = \frac{1}{2}\frac{(V_P/V_S)^2 - 2}{(V_P/V_S)^2 - 1}. \tag{24}$$

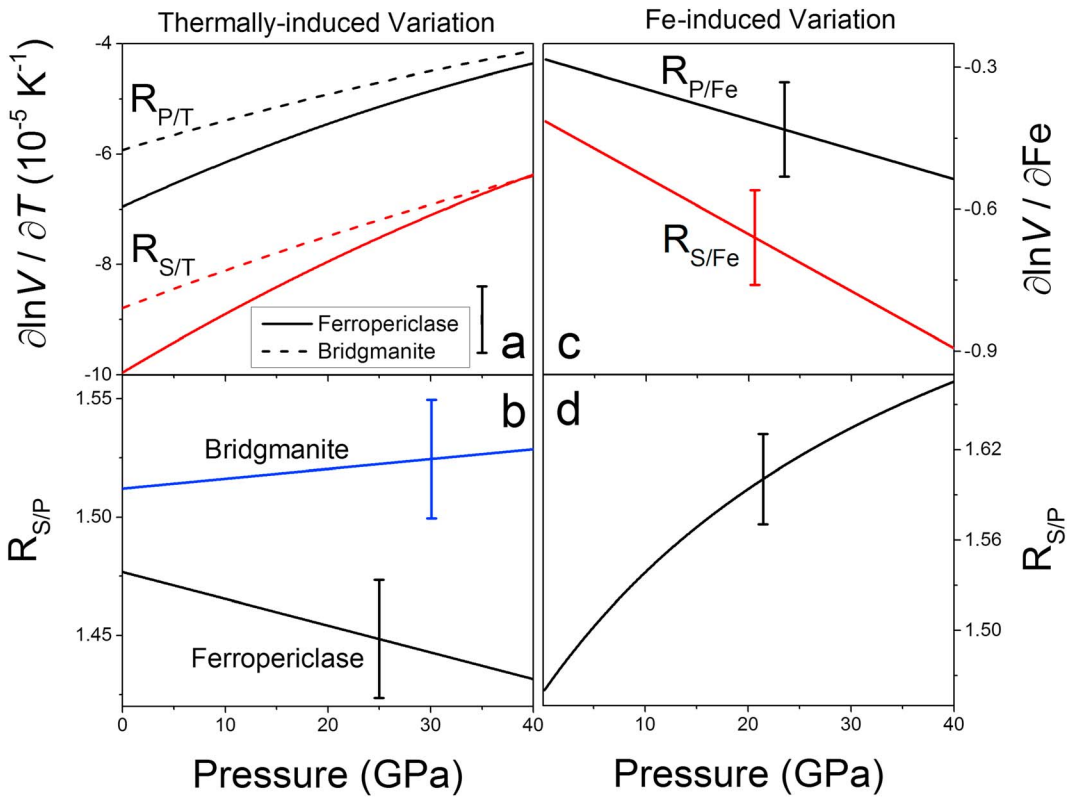

Figure 7. Pressure dependence of the thermally induced and Fe-induced lateral variation of ferropericlase $(Mg_{0.94}Fe_{0.06})O$ in the compressional and shear wave velocities along a representative geotherm [*Brown and Shankland*, 1981]. (a) $R_{P/T} = \partial \ln V_P / \partial T$ and $R_{S/T} = \partial \ln V_S / \partial T$ and (b) thermally induced heterogeneity ratio $R_{S/P} = \partial \ln V_S / \partial \ln V_P$. The dashed lines are the calculated results of bridgmanite (brg) for comparison [*Li and Zhang*, 2005]. (c) $R_{P/Fe} = \partial \ln V_P / \partial X_{Fe}$ and $R_{S/T} = \partial \ln V_S / \partial X_{Fe}$ and (d) Fe chemically induced heterogeneity ratio $R_{S/P} = \partial \ln V_S / \partial \ln V_P$. The representative error bars are estimated using standard error propagation from the modeled parameters.

Analysis of these parameters using our data shows that A decreases with increasing pressure but increases with increasing temperature (Figure 6). At ambient pressure, A is 0.39 at 300 K and 0.53 at 900 K, respectively. The anisotropy decreases to zero at both ~20 GPa, 300 K and at ~24 GPa, 900 K. As temperature was increased from 300 K to 900 K, V_P/V_S and v increased by ~2% and ~6%, respectively. Compared to MgO [*Sinogeikin and Bass*, 2000], A for fp6 is 8% higher at ambient conditions, whereas V_P/V_S and v are, respectively, increased by ~1.4% and ~7%. These results show that both addition of Fe and elevated temperature can increase elastic wave anisotropy, whereas pressure suppresses the anisotropy but increases V_P/V_S and υ at high P-T.

To apply these seismic parameters to relevant lower mantle conditions, we have also used thermoelastic modeling to calculate the V_P/V_S ratio, Poisson's ratio, and anisotropy factor to extrapolate the P-T derivatives of elastic constants along a representative lower mantle geotherm, which represents a layered mantle convection model with a reference temperature of 1873 K at 670 km depth [*Brown and Shankland*, 1981] up to 50 GPa, equivalent to a depth of 1250 km (Figures 6d–6f). The pressure range was limited to mid-lower mantle values in order to remove the effects of the Fe spin transition, which can significantly affect modeling outcomes [*Yang et al.*, 2015]. From 660 km to 1250 km, V_P/V_S varies from 1.736 to 1.760 while Poisson's ratio ranges from 0.25 to 0.26, which are generally consistent with seismic models [*Saltzer et al.*, 2004]. The anisotropy factor of ferropericlase is 0.13 at 660 km, decreases to 0 at 900 km, and then its absolute value increases monotonically with increasing pressure to 0.12 at 1250 km, suggesting that ferropericlase is highly anisotropic at depths below the mid-lower mantle.

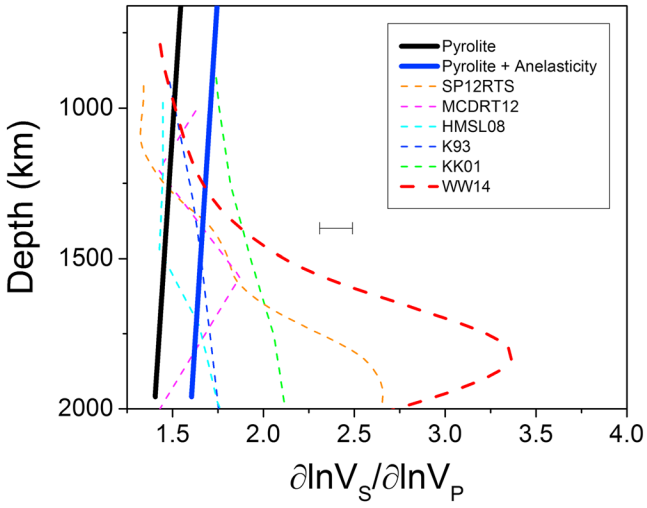

Figure 8. Depth profile of the thermally induced heterogeneity ratios ($R_{S/P} = \partial \ln V_S / \partial \ln V_P$) for a simplified pyrolite compositional model along a representative geotherm [*Brown and Shankland*, 1981]. Solid black line: simplified pyrolite model with 20% ferropericlase (fp20) and 80% bridgmanite (brg10) [*Li and Zhang*, 2005]. Solid blue line: profile corrected for anelasticity effect on the heterogeneity ratio of pyrolite. Mineral physic models for thermal lateral variations are shown as K93 with blue dashed line [*Karato*, 1993], KK01 with green dashed line [*Karato and Karki*, 2001], and WW14 with red dashed line [*Wu and Wentzcovitch*, 2014]. Seismic models are shown as magenta dashed line: MCDRT12, a normal-mode data-derived model [*Mosca et al*., 2012]; cyan dashed line: HMSL08, a model employing primarily body wave data [*Houser et al*., 2008]; orange dashed line: SP12RTS, a model derived from combined Rayleigh wave phase velocities, body wave travel times, and normal-model splitting function measurements [*Koelemeijer et al*., 2016]. The error bars are estimated using standard error propagation from the modeled parameters.

4.2. Seismic Anisotropy in the Lower Mantle

To quantify seismic anisotropy of ferropericlase under lower mantle conditions, we have calculated the V_P anisotropy (AV_P) and shear wave splitting factor (AV_S) along a representative geotherm using the following equation [*Mainprice et al*., 2000]:

$$AV_i = 100 \times \frac{V_{i,\max} - V_{i,\min}}{V_{i,\text{aggre}}}, \quad (25)$$

where $V_{i,\max}$, $V_{i,\min}$, and $V_{i,\text{aggre}}$ are the maximum, minimum, and aggregate V_P or V_S velocities. At 660 km and 1866 K, the AV_P is 4% and AV_S is 9%, and the difference between the orthogonally polarized V_{SV} and V_{SH} is 0.51 km/s. At 2000 km and 2250 K, the AV_P is 9.7% and AV_S is as high as 22.5%, whereas the difference between V_{SH} and V_{SV} is 1.6 km/s. These results show that both V_P and V_S anisotropies increase with depth and that the anisotropy of ferropericlase increases with increasing temperature at lower mantle conditions. Close to the core-mantle boundary, the splitting is expected to be even higher due to the steep thermal gradient within the *D*″ layer. The enhanced AV_P and AV_S observed here, together with the tendency of ferropericlase to develop stronger fabrics [*Yamazaki and Karato*, 2001], support the notion that ferropericlase can significantly contribute to seismic anisotropy in lowermost lower mantle.

4.3. Thermally Induced Heterogeneity Ratios Along a Lower Mantle Geotherm

The thermal or chemical origins of seismic heterogeneity can be constrained by comparing the observed ratios of various seismic parameters with mineral physics results. The ratios of first-order interest include the shear wave to compressional wave ratio ($R_{S/P} = \partial \ln V_S / \partial \ln V_P$), bulk sound to shear wave velocity ratio ($R\varphi_{/S} = \partial \ln V\varphi / \partial \ln V_S$), and density to velocity ratio ($R\rho_{/S,P} = \partial \ln \rho / \partial \ln V_{S,P}$). The contributions of these ratios to lateral heterogeneity can have thermal and/or chemical origins. Mineral physics studies have indicated that $R_{S/P} = \partial \ln V_S / \partial \ln V_P$ is less than 2–2.5 in an isochemical lower mantle, which also implies that variations in shear wave and bulk wave velocities are positively correlated [*Karato and Karki*, 2001]. Other studies have found a negative correlation between shear wave and bulk wave velocities, either throughout the entire lower mantle [*Su and Dziewonski*, 1997] or limited to the mid-lower mantle [*Masters et al*., 2000]. Most studies show that $R_{S/P}$ is ~1.5 at the top of the lower mantle and as high as 3.5 at the core-mantle boundary [*Koelemeijer et al*., 2016; *Masters et al*., 2000; *Robertson and Woodhouse*, 1996].

Here we have calculated thermally induced lateral variations in shear wave and compressional wave $\partial \ln V_{P,S} / \partial T$ for ferropericlase with 6% Fe (this study) and bridgmanite from a high P-T ultrasonic study [*Li and Zhang*, 2005] to investigate the thermal variation of these two major lower mantle minerals (Figure 7). The velocities of ferropericlase and bridgmanite were first extrapolated along the geotherm based on the derived thermoelastic parameters and finite-strain theory. The 200 K positive and negative temperature perturbations were applied to the velocities to determine the $\partial \ln V_S / \partial T$ and $\partial \ln V_P / \partial T$ for ferropericlase and bridgmanite. The pressure dependencies of $R_{S/P} = \partial \ln V_S / \partial \ln V_P$ of ferropericlase and bridgmanite are

Table 4. Thermoelastic Parameters for Ferropericlase (fp20) $(Mg_{0.8}Fe_{0.2})O$ and Bridgmanite (brg10) $(Mg_{0.9}Fe_{0.1})SiO_3$ Used in Modeling the Pyrolite Aggregate

	$(Mg_{0.8}Fe_{0.2})O$	$(Mg_{0.9}Fe_{0.1})SiO_3$
Volume percentage (%)	20	80
Density (g/cm^3)	4.101	4.217
K_S (GPa)	160	253
K_S'	4.0	4.4
$\partial Ks/\partial T$ (GPa/K)	−0.0154	−0.02
G (GPa)	102	173
G'	2.1	2.0
$\partial G/\partial T$ (GPa/K)	−0.0213	−0.028
α (K^{-1})	3.0×10^{-5}	1.9×10^{-5}

shown in Figure 8b. For ferropericlase, the $R_{S/P}$ value decreases from 1.48 at 0 GPa to 1.43 at 40 GPa. In contrast, the $R_{S/P}$ value of bridgmanite increases from 1.51 to 1.53 over the same pressure interval.

In order to compare these results with seismic models of the Earth's lower mantle, we have calculated the $R_{S/P}$ value along an expected geotherm for the simplified pyrolite model [*Brown and Shankland*, 1981] consisting of 20% ferropericlase and 80% bridgmanite [*Irifune et al*., 2010]. In order to take the effect of Fe content into account, the elastic properties of ferropericlase with XFe = 0.20 ($Mg_{0.8}Fe_{0.2}O$) were derived by assuming a linear compositional effect of FeO on elasticity of ferropericlase using data from MgO [*Sinogeikin and Bass*, 2000], $Mg_{0.94}Fe_{0.06}O$, $Mg_{0.92}Fe_{0.08}O$ [*Yang et al*., 2015], and $Mg_{0.9}Fe_{0.1}O$ [*Marquardt et al*., 2009]. Assuming that the Fe and Mg partitioning coefficient between bridgmanite (brg) and ferropericlase (fp), $K_D = \left(\frac{Fe}{Mg}\right)^{brg} / \left(\frac{Fe}{Mg}\right)^{fp} = 0.5$, is pressure independent above ~40 GPa [*Irifune et al*., 2010], thermoelastic properties of bridgmanite with XFe = 0.10 ($(Mg_{0.9}Fe_{0.10})SiO_3$) were adopted to model the velocity and seismic parameters [*Li and Zhang*, 2005]. The thermoelastic parameters used for ferropericlase and bridgmanite in the following calculations are given in Table 4.

The volume-weighted aggregate velocity profiles with depth for the simplified (excluding calcium silicate perovskite) pyrolite model are approximately consistent with preliminary reference Earth model [*Dziewonski and Anderson*, 1981] (Figure S1 in the supporting information). Positive and negative temperature perturbations by 200 K were also applied to determine the temperature variation of the aggregate velocity, $\partial \ln V_S/\partial T$ and $\partial \ln V_P/\partial T$. The $R_{S/P} = \partial \ln V_S/\partial \ln V_P$ value of the pyrolite model shows a decrease with increasing depth (Figure 8). We should note that recent studies have reported significant changes of the K_D value as a result of the spin transition, such that Fe preferentially partitions into ferropericlase [*Irifune et al*., 2010]. The effect of the spin transition on the seismic parameters needs to be further considered. Since the $R_{S/P}$ value can be significantly influenced by temperature-dependent anelasticity in the deep Earth, the predicted $R_{S/P}$ correction of ~0.2 for the anelasticity effect between 660 and 1600 km is also taken into account [*Matas and Bukowinski*, 2007] (Figure 8). Our data are consistent with most seismic observations within uncertainty for the upper part of the lower mantle including MCDRT12 [*Mosca et al*., 2012], HMSL08 [*Houser et al*., 2008], and SP12RTS [*Koelemeijer et al*., 2016]. We thus conclude that the thermal origin is dominant for the upper 1500 km of the lower mantle, which is in agreement with some seismic predictions [*Simmons et al*., 2010]. Although most of the seismic models show a high $R_{S/P}$ value in the middle part of the lower mantle [*Koelemeijer et al*., 2016; *Mosca et al*., 2012], our data did not predict such a high $R_{S/P}$ value for the high-spin ferropericlase and bridgmanite. This may suggest that other causes predominate in these regions, such as the Fe spin transition or a contribution from chemically induced heterogeneity [*Kaneshima and Helffrich*, 2010; *Simmons et al*., 2010; *Wu and Wentzcovitch*, 2014].

4.4. Effects of Fe and Fe Spin Transition on the Seismic Heterogeneity

Variation in Fe content in major lower mantle minerals is regarded as a potential chemical cause for seismic heterogeneities below the mid-lower mantle [*van der Hilst and Kárason*, 1999]. A major change in Fe partitioning between ferropericlase and bridgmanite is expected to occur in the top of the lower mantle due to the Al dissolution in bridgmanite and in the mid-lower mantle due to the Fe spin transition in ferropericlase [*Irifune et al*., 2010; *Muir and Brodholt*, 2016]. The amount of Fe in the Earth's lower mantle minerals can affect a wide range of elastic properties of the host minerals, including velocity, elastic constants, and shear modulus [*Jacobsen et al*., 2002; *Yang et al*., 2015]. Previous studies have shown that Fe substitution in ferropericlase increases its density but reduces the V_P, V_S, and shear modulus [*Jacobsen et al*., 2002, 2004], causing an anticorrelation between bulk and shear velocities, which had previously been interpreted as chemical

heterogeneity in the deep Earth [*Kellogg et al.*, 1999; *Tackley*, 2000]. For example, the effect of Fe content on seismic heterogeneity can be evaluated with $\partial \ln V_S/\partial X_{Fe} = -0.5 \pm 0.1$ and $\partial \ln V_P/\partial X_{Fe} = -0.4 \pm 0.1$, based on the experimental results at ambient pressure [*Karato and Karki*, 2001]. Here we have calculated the velocity variations with Fe content in ferropericlase ($\partial \ln V_S/\partial X_{Fe}$ and $\partial \ln V_P/\partial X_{Fe}$) to understand the potential influence of Fe variability on lateral velocity anomalies in the lower mantle. We have calculated relative variations of V_S and V_P with Fe content by considering previous elasticity data from MgO [*Sinogeikin and Bass*, 2000], ferropericlase with XFe = 0.06 (this study), ferropericlase with XFe = 0.08 [*Yang et al.*, 2015], and ferropericlase with XFe = 0.10 [*Marquardt et al.*, 2009]. At constant temperature, the calculated $\partial \ln V_S/\partial X_{Fe}$ decreases from −0.41 at 0 GPa to −0.89 at 40 GPa, while $\partial \ln V_P/\partial X_{Fe}$ decreases from −0.28 at 0 GPa to −0.54 at 40 GPa (Figures 7c and 7d). Meanwhile, $R_{S/P}$ shows an increasing trend from 1.46 at 0 GPa to 1.67 at 40 GPa, which is in contrast to the downward trending thermal variation for the lower part of lower mantle. These results indicate that chemically induced seismic heterogeneity may become dominant in the lower parts of the lower mantle. The predominance of chemically influenced heterogeneity is consistent with some seismic studies [*van der Hilst and Kárason*, 1999], especially when Fe is preferentially partitioned into ferropericlase at high pressure [*Irifune et al.*, 2010].

An alternative source of seismic heterogeneity may be the spin transition of Fe in ferropericlase in the mid-part of the lower mantle [*Wu and Wentzcovitch*, 2014]. The $R_{S/P}$ heterogeneity ratio of a homogenous pyrolite aggregate is as high as ~3.5 over the ~1500 to 2000 km depth (Figure 8), where spin crossover occurs in ferropericlase. The spin transition in ferropericlase can also produce an anticorrelation between shear wave velocity and bulk sound velocity in chemically homogeneous pyrolite aggregates, which is observed in tomography models at certain depths [*Wu and Wentzcovitch*, 2014]. Our results with high-spin ferropericlase show clear discrepancy on the $R_{S/P}$ heterogeneity ratio at depth below ~1500 km. Thus, high-spin ferropericlase alone cannot produce such a robust increase of $R_{S/P}$ value in the mid-part of the lower mantle, which implies that spin crossover of ferropericlase is a likely cause of observed lateral seismic heterogeneity in the mid-lower mantle.

Acknowledgments

We acknowledge S. Grand, C. Lu, S. Fu, and I. Yen for their constructive suggestions and discussions. We also thank Z. Mao, Y. Wu, and D. Fan for their assistance in the BLS spectra collection at 13 BMD, GSECARS. We thank GSECARS and Advanced Photon Source for providing X-ray diffraction facilities for the study. J.F.L. acknowledges support from the Geophysics and CSEDI Programs of the National Science Foundation (NSF), Carnegie-DOE Alliance Center (CDAC), and HPSTAR. S. D.J. acknowledges support from NSF EAR-0748707, the David and Lucile Packard Foundation, and the Alexander von Humboldt Foundation. GeoSoilEnviroCARS is supported by the National Science Foundation–Earth Sciences (EAR-1128799) and Department of Energy Geosciences (DE-FG02-94ER14466). The data for this paper are available by contacting the corresponding author at afu@jsg.utexas.edu.

References

Birch, F. (1947), Finite elastic strain of cubic crystals, *Phys. Rev.*, *71*(11), 809.

Birch, F. (1978), Finite strain isotherm and velocities for single-crystal and polycrystalline NaCl at high pressures and 300 K, *J. Geophys. Res.*, *83*, 1257–1268, doi:10.1029/JB083iB03p01257.

Brown, J., and T. Shankland (1981), Thermodynamic parameters in the Earth as determined from seismic profiles, *Geophys. J. R. Astron. Soc.*, *66*(3), 579–596.

Davies, D., S. Goes, and H. Lau (2015), Thermally dominated deep mantle LLSVPs: A review, in *The Earth's Heterogeneous Mantle*, pp. 441–477, Springer.

Dziewonski, A. M., and D. L. Anderson (1981), Preliminary reference Earth model, *Phys. Earth Planet. Inter.*, *25*(4), 297–356.

Every, A. (1980), General closed-form expressions for acoustic waves in elastically anisotropic solids, *Phys. Rev. B*, *22*(4), 1746.

Fei, Y., A. Ricolleau, M. Frank, K. Mibe, G. Shen, and V. Prakapenka (2007), Toward an internally consistent pressure scale, *Proc. Natl. Acad. Sci. U.S.A.*, *104*(22), 9182–9186.

Forte, A. M. (2000), Seismic-geodynamic constraints on mantle flow: Implications for layered convection, mantle viscosity, and seismic anisotropy in the deep mantle, in *Earth's Deep Interior: Mineral Physics and Tomography from the Atomic to the Global Scale*, edited by F. D. Amir Khan, pp. 441–477, Springer, New York.

Forte, A. M., R. L. Woodward, and A. M. Dziewonski (1994), Joint inversions of seismic and geodynamic data for models of three-dimensional mantle heterogeneity, *J. Geophys. Res.*, *99*, 21,857–21,877, doi:10.1029/94JB01467.

Garnero, E. J., and A. K. McNamara (2008), Structure and dynamics of Earth's lower mantle, *Science*, *320*(5876), 626–628.

Hager, B. H., R. W. Clayton, M. A. Richards, R. P. Comer, and A. M. Dziewonski (1984), Lower mantle heterogeneity, dynamic topography and the geoid, *Nature*, *313*(14), 541–545.

Hill, R. (1952), The elastic behaviour of a crystalline aggregate, *Proc. Phys. Soc. A*, *65*, 349.

Houser, C., G. Masters, P. Shearer, and G. Laske (2008), Shear and compressional velocity models of the mantle from cluster analysis of long-period waveforms, *Geophys. J. Int.*, *174*(1), 195–212.

Irifune, T., T. Shinmei, C. A. McCammon, N. Miyajima, D. C. Rubie, and D. J. Frost (2010), Iron partitioning and density changes of pyrolite in Earth's lower mantle, *Science*, *327*(5962), 193–195.

Jackson, J. M., J. Zhang, J. Shu, S. V. Sinogeikin, and J. D. Bass (2005), High-pressure sound velocities and elasticity of aluminous $MgSiO_3$ perovskite to 45 GPa: Implications for lateral heterogeneity in Earth's lower mantle, *Geophys. Res. Lett.*, *32*, L21305, doi:10.1029/2005GL023522.

Jackson, J. M., S. V. Sinogeikin, S. D. Jacobsen, H. J. Reichmann, S. J. Mackwell, and J. D. Bass (2006), Single-crystal elasticity and sound velocities of $(Mg_{0.94}Fe_{0.06})O$ ferropericlase to 20 GPa, *J. Geophys. Res.*, *111*, B09203, doi:10.1029/2005JB004052.

Jacobsen, S. D., H.-J. Reichmann, H. A. Spetzler, S. J. Mackwell, J. R. Smyth, R. J. Angel, and C. A. McCammon (2002), Structure and elasticity of single-crystal (Mg,Fe)O and a new method of generating shear waves for gigahertz ultrasonic interferometry, *J. Geophys. Res.*, *107*(B2), 2037, doi:10.1029/2001JB000490.

Jacobsen, S. D., H. Spetzler, H. J. Reichmann, and J. R. Smyth (2004), Shear waves in the diamond-anvil cell reveal pressure-induced instability in (Mg, Fe)O, *Proc. Natl. Acad. Sci. U.S.A.*, *101*(16), 5867–5871.

Jacobsen, S. D., H. J. Reichmann, A. Kantor, and H. A. Spetzler (2005), A gigahertz ultrasonic interferometer for the diamond anvil cell and high-pressure elasticity of some iron-oxide minerals, in *Advances in High-Pressure Technology for Geophysical Applications*, edited by J. Chen et al., pp. 25–48, Elsevier, Amsterdam.

Kaneshima, S., and G. Helffrich (2010), Small scale heterogeneity in the mid-lower mantle beneath the circum-Pacific area, *Phys. Earth Planet. Inter.*, *183*(1), 91–103.

Kantor, I., V. Prakapenka, A. Kantor, P. Dera, A. Kurnosov, S. Sinogeikin, N. Dubrovinskaia, and L. Dubrovinsky (2012), BX90: A new diamond anvil cell design for X-ray diffraction and optical measurements, *Rev. Sci. Instrum.*, *83*(12), 125102.

Karato, S. (1993), Importance of anelasticity in the interpretation of seismic tomography, *Geophys. Res. Lett.*, *20*, 1623–1626, doi:10.1029/93GL01767.

Karato, S., and B. B. Karki (2001), Origin of lateral variation of seismic wave velocities and density in the deep mantle, *J. Geophys. Res.*, *106*, 21,771–21,783, doi:10.1029/2001JB000214.

Karki, B. B., L. Stixrude, S. J. Clark, M. C. Warren, G. J. Ackland, and J. Crain (1997), Structure and elasticity of MgO at high pressure, *Am. Mineral.*, *82*(1), 51–60.

Karki, B., R. Wentzcovitch, S. De Gironcoli, and S. Baroni (1999), First-principles determination of elastic anisotropy and wave velocities of MgO at lower mantle conditions, *Science*, *286*(5445), 1705–1707.

Kellogg, L. H., B. H. Hager, and R. D. van der Hilst (1999), Compositional stratification in the deep mantle, *Science*, *283*(5409), 1881–1884.

Koelemeijer, P., J. Ritsema, A. Deuss, and H.-J. van Heijst (2016), SP12RTS: A degree-12 model of shear-and compressional-wave velocity for Earth's mantle, *Geophys. J. Int.*, *204*(2), 1024–1039.

Li, B., and J. Zhang (2005), Pressure and temperature dependence of elastic wave velocity of $MgSiO_3$ perovskite and the composition of the lower mantle, *Phys. Earth Planet. Inter.*, *151*(1–2), 143–154, doi:10.1016/j.pepi.2005.02.004.

Mainprice, D., G. Barruol, and W. B. Ismail (2000), The seismic anisotropy of the Earth's mantle: From single crystal to polycrystal, in *Earth's Deep Interior: Mineral Physics and Tomography from the Atomic to the Global Scale*, *Geophys. Monogr.*, vol. 117, pp. 237–264, AGU, Washington, D. C.

Marquardt, H., S. Speziale, H. J. Reichmann, D. J. Frost, and F. R. Schilling (2009), Single-crystal elasticity of $(Mg_{0.9}Fe_{0.1})O$ to 81 GPa, *Earth Planet. Sci. Lett.*, *287*(3–4), 345–352.

Masters, G., G. Laske, H. Bolton, and A. Dziewonski (2000), The relative behavior of shear velocity, bulk sound speed, and compressional velocity in the mantle: Implications for chemical and thermal structure, in *Earth's Deep Interior: Mineral Physics and Tomography from the Atomic to the Global Scale*, pp. 63–87.

Matas, J., and M. S. Bukowinski (2007), On the anelastic contribution to the temperature dependence of lower mantle seismic velocities, *Earth Planet. Sci. Lett.*, *259*(1), 51–65.

McCammon, C., I. Kantor, O. Narygina, J. Rouquette, U. Ponkratz, I. Sergueev, M. Mezouar, V. Prakapenka, and L. Dubrovinsky (2008), Stable intermediate-spin ferrous iron in lower-mantle perovskite, *Nat. Geosci.*, *1*(10), 684–687, doi:10.1038/ngeo309.

Mosca, I., L. Cobden, A. Deuss, J. Ritsema, and J. Trampert (2012), Seismic and mineralogical structures of the lower mantle from probabilistic tomography, *J. Geophys. Res.*, *117*, B06304, doi:10.1029/2011JB008851.

Muir, J. M. R., and J. P. Brodholt (2016), Ferrous iron partitioning in the lower mantle, *Phys. Earth Planet. Inter.*, *257*, 12–17, doi:10.1016/j.pepi.2016.05.008.

Poirier, J.-P. (2000), *Introduction to the Physics of the Earth's Interior*, Cambridge Univ. Press, Cambridge, U. K.

Ringwood, A. E. (1975), *Composition and Petrology of the Earth's Mantle*, McGraw-Hill, New York.

Robertson, G., and J. Woodhouse (1996), Ratio of relative *S* to *P* velocity heterogeneity in the lower mantle, *J. Geophys. Res.*, *101*, 20,041–20,052, doi:10.1029/96JB01905.

Saltzer, R. L., E. Stutzmann, and R. D. van der Hilst (2004), Poisson's ratio in the lower mantle beneath Alaska: Evidence for compositional heterogeneity, *J. Geophys. Res.*, *109*, B06301, doi:10.1029/2003JB002712.

Simmons, N. A., A. M. Forte, L. Boschi, and S. P. Grand (2010), GyPSuM: A joint tomographic model of mantle density and seismic wave speeds, *J. Geophys. Res.*, *115*, B12310, doi:10.1029/2010JB007631.

Sinogeikin, S. V., and J. D. Bass (2000), Single-crystal elasticity of pyrope and MgO to 20 GPa by Brillouin scattering in the diamond cell, *Phys. Earth Planet. Inter.*, *120*(1–2), 43–62.

Speziale, S., and T. Duffy (2002), Single-crystal elastic constants of fluorite (CaF 2) to 9.3 GPa, *Phys. Chem. Miner.*, *29*(7), 465–472.

Su, W.-j., and A. M. Dziewonski (1997), Simultaneous inversion for 3-D variations in shear and bulk velocity in the mantle, *Phys. Earth Planet. Inter.*, *100*(1), 135–156.

Tackley, P. J. (2000), Mantle convection and plate tectonics: Toward an integrated physical and chemical theory, *Science*, *288*(5473), 2002–2007.

Tange, Y., Y. Nishihara, and T. Tsuchiya (2009), Unified analyses for P-V-T equation of state of MgO: A solution for pressure-scale problems in high P-T experiments, *J. Geophys. Res.*, *114*, B03208, doi:10.1029/2008JB005813.

Tsuchiya, T. (2011), Elasticity of subducted basaltic crust at the lower mantle pressures: Insights on the nature of deep mantle heterogeneity, *Phys. Earth Planet. Inter.*, *188*(3), 142–149.

van der Hilst, R. D., and H. Kárason (1999), Compositional heterogeneity in the bottom 1000 kilometers of Earth's mantle: Toward a hybrid convection model, *Science*, *283*(5409), 1885–1888.

Wu, Z., and R. M. Wentzcovitch (2014), Spin crossover in ferropericlase and velocity heterogeneities in the lower mantle, *Proc. Natl. Acad. Sci. U.S.A.*, *111*(29), 10,468–10,472.

Wu, Z., J. F. Justo, and R. M. Wentzcovitch (2013), Elastic anomalies in a spin-crossover system: Ferropericlase at lower mantle conditions, *Phys. Rev. Lett.*, *110*, 228,501.

Yamazaki, D., and S.-i. Karato (2001), Some mineral physics constraints on the rheology and geothermal structure of Earth's lower mantle, *Am. Mineral.*, *86*(4), 385–391.

Yamazaki, D., and S.-i. Karato (2002), Fabric development in (Mg,Fe)O during large strain, shear deformation: Implications for seismic anisotropy in Earth's lower mantle, *Phys. Earth Planet. Inter.*, *131*(3–4), 251–267, doi:10.1016/S0031-9201(02)00037-7.

Yang, J., X. Tong, J.-F. Lin, T. Okuchi, and N. Tomioka (2015), Elasticity of ferropericlase across the spin crossover in the Earth's lower mantle, *Sci. Rep.*, *5*, 17,188.